Supporting Information

Ab Initio Molecular Dynamics Reveals New Metal-Binding Sites in Atomically Dispersed Pt_1/TiO_2 catalysts

Nicholas Humphrey,† Selin Bac,† and Shaama Mallikarjun Sharada*,†,‡

†*Mork Family Department of Chemical Engineering and Materials Science, University of Southern California, Los Angeles CA, USA 90089*

‡*Department of Chemistry, University of Southern California, Los Angeles CA, USA 90089*

E-mail: ssharada@usc.edu

Methods

Model construction: The (110) surface of rutile is modeled using a 5-layer, 2x4 unit cell with a vacuum of 12Å. The unit cell size is chosen such that Pt atoms in repeating images are separated by at least 10Å. The top layer is relaxed in all simulations. The pristine (reduced) surface consists of 240 (238) atoms. Oxygen vacancies are created by removing the surface basal/bridged O atom and the corresponding O atom at the bottom of the unit cell.[1]

Density functional theory: All spin polarized calculations are performed using Vienna Ab Initio Simulation Package, VASP 5.4,[2–5] using the SCAN meta-generalized gradient approximation (meta-GGA).[6] The Atomic Simulation Environment (ASE) is utilized for model construction and geometry relaxation (threshold=$0.05eV/$Å).[7] All atoms are described using the default projector augmented wave (PAW) potentials available in VASP: Ti containing four, O containing six, and Pt containing ten valence electrons.[8,9] The non-spherical contributions related to the gradient of the density in the PAW spheres are included in the calculations

with the d-orbitals included in the kinetic energy density mixing. Electronic relaxations are carried out using the preconditioned conjugate gradient algorithm recommended for meta-GGA functionals. The Brillouin Zone is integrated using the Monkhorst-Pack set of k-points: an (8x8x8) mesh for the bulk calculations. Gaussian smearing ($\sigma = 0.1eV$) is used along with cutoff energies of 1000eV, 400eV, and 200eV for bulk, DFT, and AIMD calculations, respectively. We report binding energies calculated using Γ-point sampling since (with 400eV cutoff) they are in good agreement with the (2x3x1) k-point mesh. We employ Bader analysis to calculate charges on surface atoms.[10,11] Binding energies (BE) are calculated using reference energies of gas phase Pt atom and bare pristine or reduced (110) surface (TiO_x):

$$BE = E_{Pt/TiO_x} - E_{TiO_x} - E_{Pt} \tag{1}$$

We analyze the effects of including both dipole corrections[12,13] as well as dispersion interactions on binding energies. Shown in Table S1, dipole corrections are typically small and therefore do not affect trends in binding energies across sites. Table S1 also shows dispersion corrections to binding energies calculated using Grimme's D3 method with the Becke-Johnson damping function.[14,15] In general, dispersion interactions are more favorable for basal sites - H1, H2, Ti5c, and O_{ba} - and contribute less to stabilization of sites located on the bridge (O_{br} and Ti6c). Since the inclusion of dispersion corrections does not alter our main conclusions in this work, the results reported here do not account for dispersion. Table S2 shows the justification for choice of 400eV as cutoff energy.

Table S1: Contributions from dipole and dispersion corrections to Pt BEs for sites reported in Figure 1 of the paper.

Site	H1	H2	Ti5c	O_{ba}	O_{br}	Ti6c	$O_{ba,vac}$	$O_{br,vac}$
ΔE_{dipole}	0.03	0.01	0.03	0.04	0.04	0.08	0.02	0.03
$\Delta E_{dispersion}$	-0.45	-0.51	-0.44	-0.51	-0.28	-0.35	-0.37	0.54

Ab initio molecular dynamics: AIMD trajectories are initiated from previously determined DFT binding sites. We simulate several shorter (2ps) trajectories rather than a

Table S2: Sensitivity of BEs to choice of cutoff energy.

Site	H1	H2	Ti5c	O_{ba}	O_{br}	Ti6c	$O_{ba,vac}$	$O_{br,vac}$
200eV	-1.89	-1.77	-0.89	-7.91	-0.16	+2.46	-4.40	-2.55
300eV	-1.87	-1.79	-1.02	-1.39	-1.35	-1.86	-3.99	-2.75
400eV	-2.37	-1.83	-1.02	-2.37	-1.49	-1.99	-4.09	-2.72
500eV	-2.27	-1.82	-1.02	-2.24	-1.42	-1.91	-4.09	-2.71

single, very long trajectory. This is because some diffusion barriers (e.g. basal-to-bridge migration)[16] are not easily overcome even at 1200K. It is therefore unlikely that, even at longer timescales, a single trajectory successfully samples all possible metal-binding configurations on the surface. Smaller cutoff energies (200eV) are employed to enable computationally efficient sampling along with the (2x3x1) k-point mesh because the geometries of the structures do not change significantly with increasing cutoff energy. Symmetry is turned off for all calculations. The simulation protocol for identification of new sites involves five steps:

1. **Temperature ramp**: The DFT-optimized geometries are heated at a rate of 500K/ps from 10K to 1200K. The velocities are scaled at every 2.0fs timestep and 40 steps are stored in the Broyden mixer.

2. **Equilibration**: The temperature ramp is followed by a short NVT equilibration step (250fs). We use the Nosé-Hoover thermostat[17] and calculate the stress tensor at a timestep of 1.0fs. Ten steps are stored in the Broyden mixer.

3. **NVE Ensemble**: Two picosecond trajectories are initiated from the equilibrated structures with a 1fs timestep. Settings for mixing and electronic calculations are identical to the equilibration step.

4. **DFT Relaxation**: AIMD snapshots are identified based on a combination of changes in $n_{O/Ti}$, local energy minima, and visible changes to the surface. The structures are relaxed to local minima using DFT with Γ-point sampling and 400eV cutoff energies.

5. **Barrier to site formation**: An additional validation step is necessary to examine whether the new sites formed at elevated AIMD temperatures are accessible at lower

reaction temperatures. By hypothesizing that the largest barriers must be associated with significant metal and support atom displacements from the parent site, we choose a subset of sites exhibit these characteristics. Nudged elastic band (NEB)[18–20] calculations, with four images between initial and final structures (400eV cutoff energies), are carried out to determine the barrier to formation of the new sites from their parent sites.

Trajectories are visualized using the Ovito software package.[21] Owing to electronic convergence issues, bare $O_{ba,vac}$ surface and Pt-bound $O_{ba,vac}$ simulations are carried out with Γ-point sampling. AIMD simulations are not performed for the Pt-binding point obtained at O_{br} owing to issues with electronic convergence. We note that the AIMD simulations for the Ti5c site are initiated at a site with the Pt off-center from the Ti5c position. This is because all AIMD trajectories are initiated from structures generated using the block-Davidson electronic relaxation algorithm. This algorithm leads to small geometry differences only for the Ti5c site. The preconditioned conjugate gradient algorithm is subsequently employed for DFT relaxation of all AIMD snapshots.

We note that an additional step is involved in obtaining the AIMD-identified **A5** site. Although the Pt atom is in the vicinity of the Ti5c site on the reduced surface between 500 and 750ps (Figure 2(g) of the paper), obtaining a converged **A5** geometry using AIMD snapshots as guesses is challenging because calculations typically converge to the neighboring O_{ba} site (**A6**). Therefore, we initiate a separate DFT relaxation calculation with Pt at the Ti5c site on a surface containing a bridged oxygen vacancy to obtain **A5**.

DFT: Bare and Pt-bound Surfaces

Bulk properties: The lattice parameters (a, c) for rutile TiO_2 are (4.598Å, 2.960Å). The parameters are in good agreement with both experiment (4.593Å, 2.958Å) and prior SCAN studies (4.609Å, 2.956Å).[22]

Geometries – Bare surfaces: Relaxed structures of the bare pristine and reduced surfaces are shown in Figure S1. Note that the basal oxygen adjacent to the basal vacancy (Figure S1(b)) migrates to the mid-point between two basal sites upon optimization with DFT.

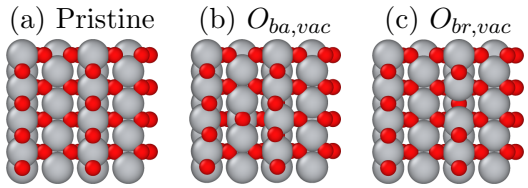

Figure S1: SCAN geometries of bare rutile (110) surfaces.

Ti5c vacancy site: WGS kinetics studies show that CO binds strongly to cationic Pt sites created via surface doping of Pt at Ti5c vacancies.[23] However, we do not carry out AIMD simulations at this site (Figure S2) because Pt binds very strongly to the vacancy site and the barrier to leave this site will likely not be overcome at 1200K.

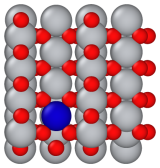

Figure S2: Pt doped at Ti5c vacancy site: BE = -10.40eV, magnetic moment = $4.00\mu_B$, Pt charge = +1.53e.

Vibrational analysis: The Vibrations package in ASE is utilized to calculate finite difference Hessian matrices (displacement = 0.01Å) for the Pt-bound surfaces. At each site, with the exception of Pt and its nearest neighbors, all other atoms are frozen. The resulting vibrational frequencies are reported in Table S3.

Table S3: Vibrational modes for Pt binding on rutile $TiO_2(110)$ surface. Note that if a site geometry possesses small imaginary frequency $< 50cm^{-1}$, it is classified as a minimum.

Site	Vibrational frequencies (cm^{-1})
H1	49.6, 73.2, 107.1, 268.4, 275.7, 351.5, 361.8, 440.4, 641.8
H2	44.9i, 48.1, 129.1, 244.5, 312.3, 318.8, 360.5, 383.8, 464.3
Ti5c	46.6i, 43.3i, 75.9, 234.4, 344.5, 345.8
O_{ba}	49.0, 55.1, 102.1, 231.6, 278.5, 284.8, 322.8, 333.6, 344.1, 370.5, 390.2, 424.9, 466.9, 540.6, 656.9
O_{br}	51.1, 84.3, 117.7, 216.4, 263.6, 288.5, 321.2, 334.4, 428.3
Ti6c	43.2, 78.3, 116.5, 234.4, 251.6, 284.6, 302.4, 304.2, 335.7, 346.7, 709.2, 721.3
$O_{ba,v}$	91.8, 95.7, 117.7, 260.2, 287.9, 306.7, 329.7, 336.3, 349.3, 388.1, 400.1, 423.5, 428.8, 445.7, 526.9, 564.0, 583.5, 619.9
$O_{br,v}$	51.1, 84.3, 117.7, 216.4, 263.6, 288.5, 321.2, 334.4, 428.3
A1	66.1, 100.3, 125.1, 171.4, 172.8, 260.0, 301.0, 324.0, 366.8, 388.9, 439.7, 442.9, 659.0, 724.3, 749.3
A2	95.4, 99.9, 112.0, 244.2, 281.5, 300.8, 306.4, 336.3, 353.1, 384.0, 397.7, 419.7, 452.1, 466.3, 551.2, 571.5, 591.8, 618.3
A3	90.9, 98.7, 122.4, 222.1, 309.4, 329.2, 332.8, 340.5, 378.6, 382.6, 402.0, 456.1
A4	52.1, 66.8, 94.5, 241.4, 285.5, 346.1, 350.8, 452.4, 508.7
A5	32.7, 40.0, 89.9, 264.8, 347.1, 403.9
A6	36.3, 51.4, 89.7, 242.6, 275.6, 298.5, 334.7, 361.2, 368.2, 384.4, 395.4, 455.2, 468.9, 559.5, 653.5
A7	42.8, 71.6, 98.6, 248.4, 269.5, 273.8, 295.3, 301.8, 334.3, 353.5, 374.4, 387.4, 461.6, 494.1, 595.3
A8	46.2, 52.6, 102.0, 254.2, 293.8, 305.0, 365.2, 380.1, 471.2

LDOS Analysis

Bare surface: Local density of states (LDOS) for both bare and Pt-bound surfaces, projected on nearest atoms to Pt, are shown in Figures S3-S5. On the pristine surface (Figure S3(a)), 2p orbitals of oxygen atoms constitute valence bands and titanium 3d orbitals constitute conduction bands.[24,25] With the removal of oxygen atoms, the surface is reduced and two unpaired electrons are localized at the 3d orbitals of Ti5c atoms (Figure S3(b) and (c)). Since we symmetrically remove the oxygen atoms from the top and bottom of the slab, the magnetic moments of vacancy sites are approximately 4. These additional electrons on the TiO_2 surface cause a shift in the Fermi level towards the conduction band.[26–28]

DFT sites – H1, H2, Ti5c, O_{ba}, O_{br}, Ti6c, $O_{ba,vac}$, $O_{br,vac}$: LDOS plots are shown in Figure S4. At the H1, H2 and O_{ba} sites, there are no unpaired electrons as the surface is stoichiometric and Pt 5d and 6s orbitals are fully occupied. Pt is located closest to a bridged oxygen atom at the H1 and basal oxygen at the H2 and O_{ba} sites. Therefore, bond formation occurs due to overlap between bridged oxygen 2p with Pt 5d orbitals at the H1 site and overlap with basal oxygen 2p orbitals at the H2 and O_{ba} sites. The conduction band shows overlap between Pt 6s orbitals and 3d orbitals of nearest Ti neighbors. The similarities in LDOS, nearest-neighbor distances, and magnetic moments translates to nearly identical Pt binding energies at the H1 and O_{ba} sites. The H1 LDOS obtained in this study is in

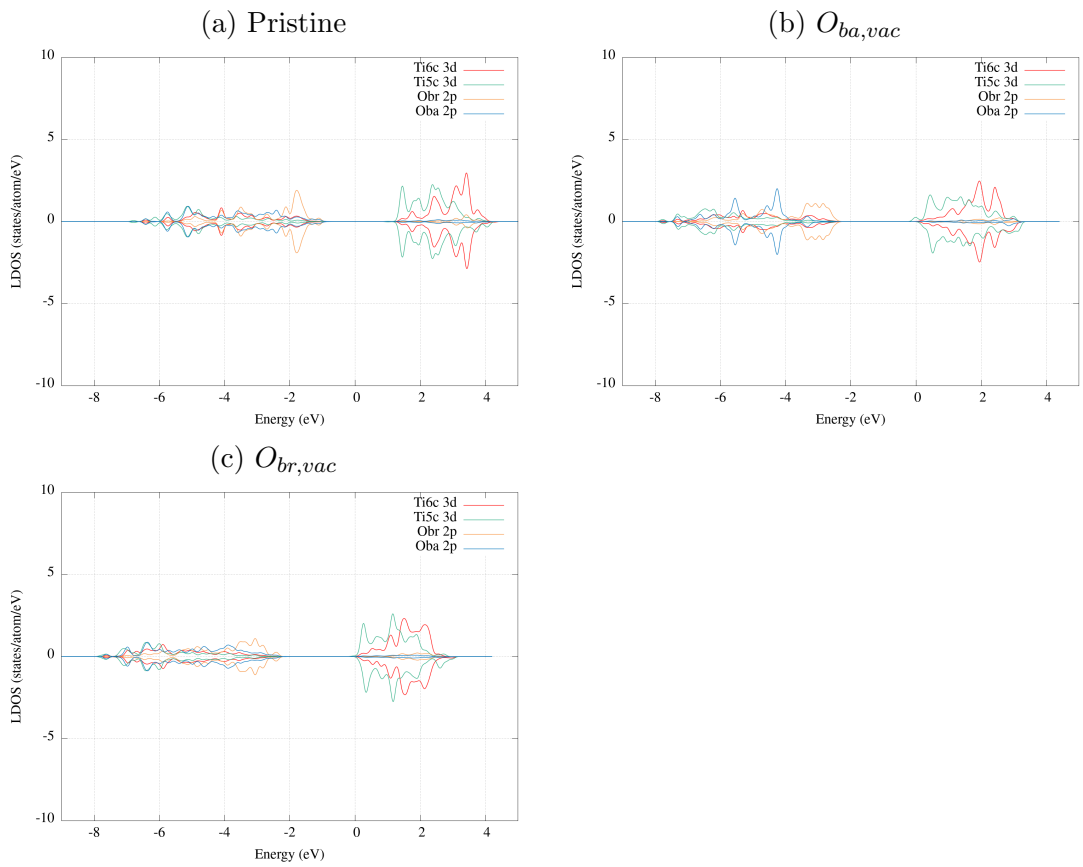

Figure S3: Local density of states analysis for the bare pristine and reduced surfaces.

qualitative agreement with that reported by Matsunaga et al.[29] Although the total DOS for Ti5c is symmetric in up/down densities, the LDOS exhibits small asymmetries, possibly due to Pt-binding with subsurface atoms that are not accounted for in the LDOS. Overlaps between Pt and bridged oxygen orbitals explain the displacement of both adjacent bridged oxygen atoms towards Pt. Owing to greater Pt-O distances compared to H1 and O_{ba}, orbital overlap and consequently Pt affinities are weaker at H2 and Ti5c. Strong binding of Pt at H2 compared to Ti5c site results from the greater overlap between Pt 5d and 6s orbitals and basal oxygen 2p orbitals observed in H2 site just below the Fermi level.

The small negative magnetic moments at the O_{br} and Ti6c sites are caused by both nearest neighbors as well as partially filled Pt 5d orbitals resulting from charge transfer to the support. The magnetic moment originates in both unpaired electrons on the Pt atom, likely

caused by retention of the d^9s^1 ground state electronic configuration, and its nearest neighbors. The small magnetic moments at these two sites are caused by both nearest neighbors as well as partially filled Pt 5d orbitals resulting from charge transfer to the support. Overlaps between the Pt 5d, bridged oxygen 2p and 6-coordinated Ti atom 3d orbitals are evident in O_{br} site near the Fermi level. Strong overlap is observed across energy levels between Pt valence orbitals and 2p orbitals of the closest two bridged oxygen atoms in Ti6c site.

At the $O_{br,vac}$ site, Pt 5d and 6s orbitals are fully occupied. The net magnetic moment at the site originates in the unpaired electrons at the bottom of the cell where the mirroring oxygen atom is removed during vacancy creation. This induces a negative charge on the Pt atom. However, since Pt is fully occupied, there is less overlap between Pt 5d and 6s with the orbitals of the neighboring atoms. Therefore Pt-binding is significantly weaker at $O_{br,vac}$ compared to the $O_{ba,vac}$ site. This is similar to a prior study, which shows that electrons in a bridged oxygen vacancy site are readily transferred to the Pt atom compared to the $O_{ba,vac}$ site.[29] However, our results differ from this study near the Fermi level. While the earlier study reports hybridization between 3d orbitals of Ti5c and Pt, we observe only a small peak at the Fermi level by the Ti5c 3d orbital with no noticeable overlap.

AIMD sites – A1-A8: The LDOS plots for all the new sites emerging from AIMD trajectories are reported in Figure S5. LDOS plots verify that the electronic configurations of all sites are distinct from their parent sites as well as each other. Stronger binding at the **A1** site compared to its parent Ti6c originates in greater overlap between Pt 5d orbitals and O_{br} 2p states close to the Fermi level. The **A2** site has four unpaired electrons similar to its parent $O_{ba,vac}$ site, results in a shift of the Fermi level towards the conduction band. There is an additional Pt 6s overlap with Ti 3d orbitals in the (-2)–0eV region of A2 LDOS, not observed in $O_{ba,vac}$, which likely leads to stronger Pt-binding at this site. Even stronger binding is observed at **A3** owing to overlap between Pt 6s and 5d and valence orbitals of

both O and Ti nearest neighbors. Owing to lower magnetic moment of this site compared to $O_{ba,vac}$ and **A2**, the Fermi level is in the middle of conduction and valence bands. Sites **A4**, **A6**–**A8** have four unpaired electrons each, unlike two electrons in the parent $O_{br,vac}$. All of these sites have lower Pt affinity compared to the parent owing to less overlap between Pt and nearest neighbor support atoms. With the exception of **A6**, overlaps occur close to the Fermi level. Overlaps between Pt 5d, Ti5c 3d and O_{ba} 2p orbitals in **A5** near -2eV results in stronger binding of Pt compared to **A4**, **A6**–**A8**.

CO Adsorption

CO-bound geometries are relaxed to local minima using the procedure described in Section 1, with Γ-point sampling and 400eV cutoff energies. Table S4 reports binding energies of Pt and CO at all sites (except H2, Ti5c, **A5** and **A8**), together with CO stretching frequencies. Binding energies of Pt and CO are both calculated with reference to the gas phase atom/molecule. The binding energy of CO is calculated as the difference between the CO-bound site (E_{CO-Pt/TiO_x}) and sum of the binding site (E_{Pt/TiO_x}) and gas phase CO (E_{CO}). The binding energy results are plotted in Figure 5 of the paper. Only CO and Pt atoms are considered in the calculation of frequencies. CO stretching frequencies of the adsorbed sites are red-shifted from calculated CO gas molecule frequency (2171.9cm^{-1}), in line with prior experimental and computational studies.[23,30–33] While there are no reported IR spectra for CO adsorbed on $Pt_1/TiO_2(110)$ (rutile) to the best of our knowledge, our work is in agreement with anatase studies that report IR bands at ∼2100cm^{-1}.[33]

AIMD Simulations

Table S5 reports time-averaged temperature, Pt coordination number, and site proximity of the Pt atom. We note that since these are short trajectories, the results do not represent true ensemble averages. In addition to NVE outcomes reported in Figures 2 and 3 of the paper, Figure S6 reports variation of system temperature (top subplot) and potential energies

Table S4: Pt and CO binding energies (BE, eV) and stretching frequencies of CO (ω_{CO}).

Site	BE, Pt	BE, CO	ω_{CO} (cm^{-1})
H1	-2.37	-3.88	2128.6
O_{ba}	-2.37	-3.58	2136.4
O_{br}	-1.49	-3.26	2134.0
Ti6c	-1.99	-3.16	2080.6
$O_{ba,vac}$	-4.09	-0.62	2139.4
$O_{br,vac}$	-2.72	-3.46	2109.8
A1	-2.35	-3.01	2137.2
A2	-4.13	-0.43	2125.9
A3	-4.55	-1.67	2138.4
A4	-2.26	-3.85	2120.9
A6	-2.32	-3.61	2131.8
A7	-2.54	-3.40	2131.6

(bottom subplot) in the NVE trajectory.

Table S5: NVE time-averaged quantities: Temperature ($\overline{T}$), Pt coordination numbers for O ($\overline{n_O}$) and Ti ($\overline{n_{Ti}}$), and the nearest DFT-optimized site ($\overline{Site}$).

Site	$\overline{T}$ (K)	$\overline{n_O}$	$\overline{n_{Ti}}$	$\overline{Site}$
H1	1256.9	0.89	0.90	H1
H2	1255.8	0.89	0.76	O_{ba}
Ti5c	1091.6	0.87	0.69	H1
O_{ba}	1122.1	0.88	0.77	H1
Ti6c	1128.5	1.72	1.06	Ti6c
$O_{ba,vac}$	1212.4	0.59	2.47	$O_{ba,vac}$
$O_{br,vac}$	1053.0	0.52	1.06	O_{ba}

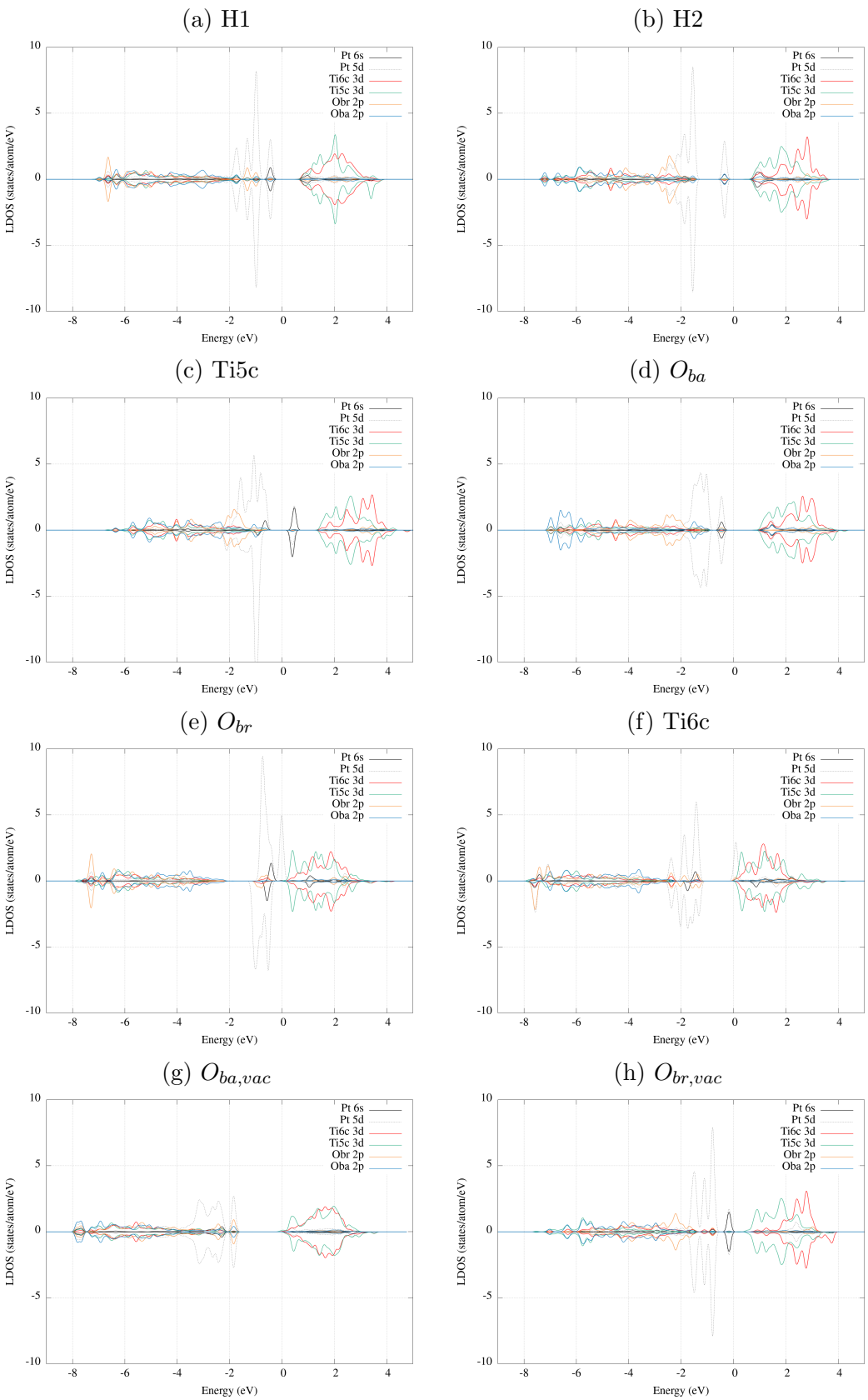

Figure S4: LDOS analysis for all sites reported in Figure 1 of the paper.

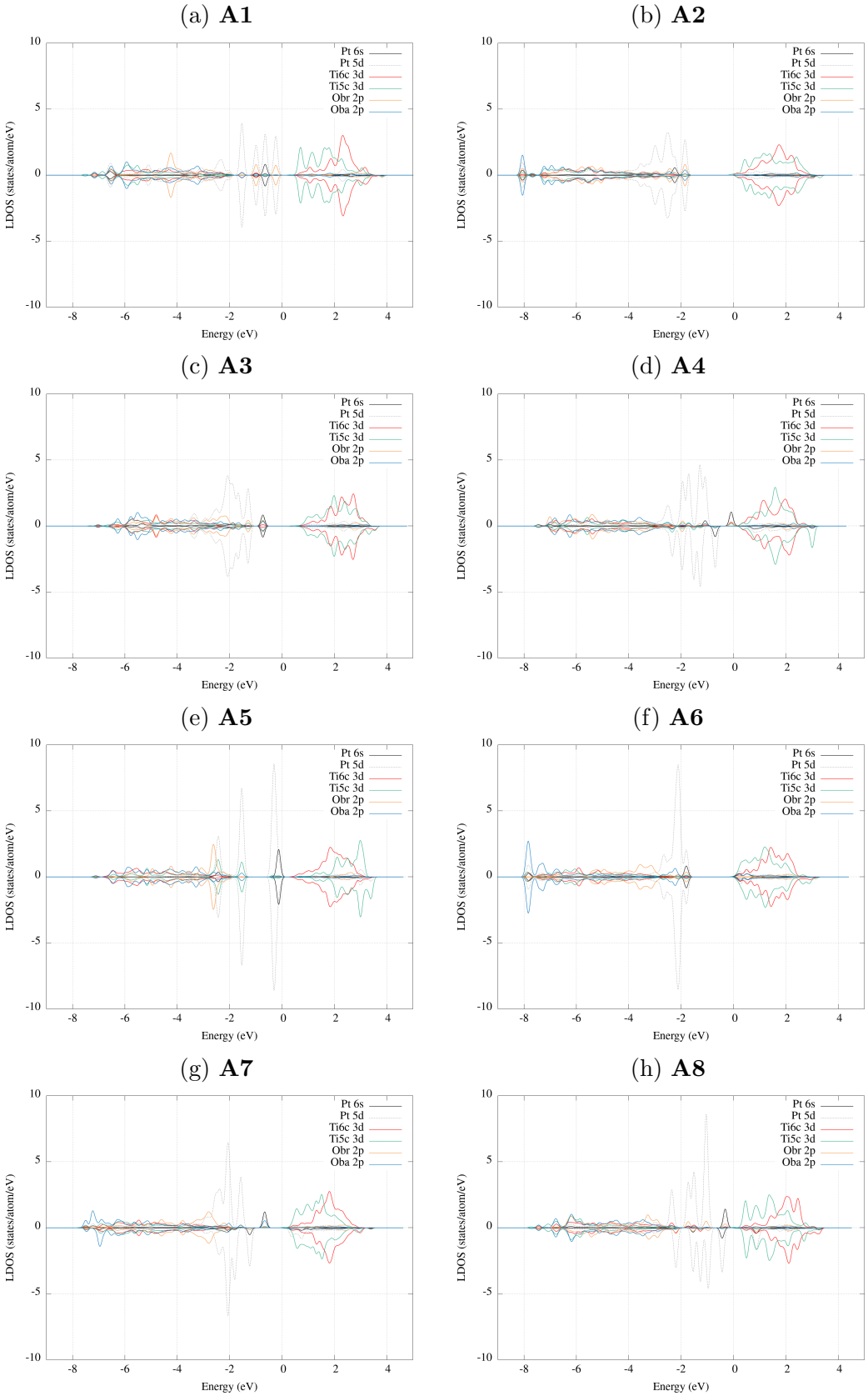

Figure S5: LDOS analysis for new sites determined from AIMD trajectories, reported in Figure 4 of the paper.

(a) H1

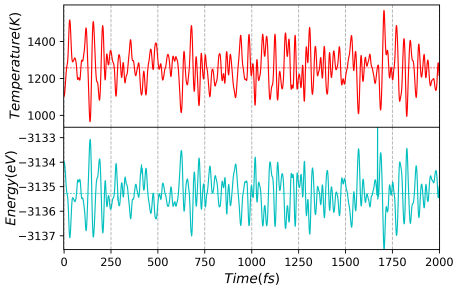

(b) H2

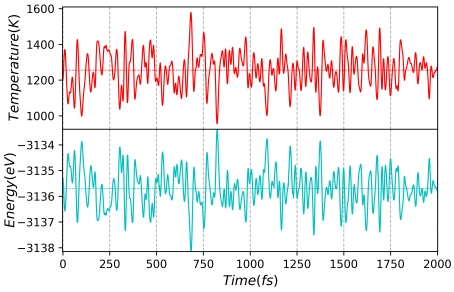

(c) Ti5c*

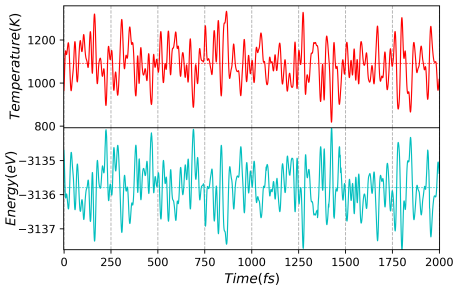

(d) O_{ba}

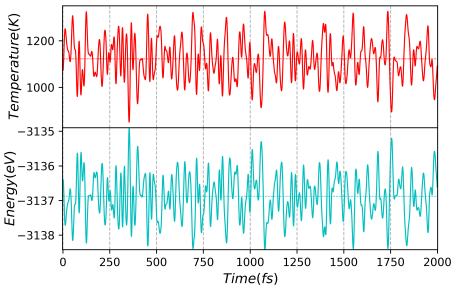

(e) Ti6c

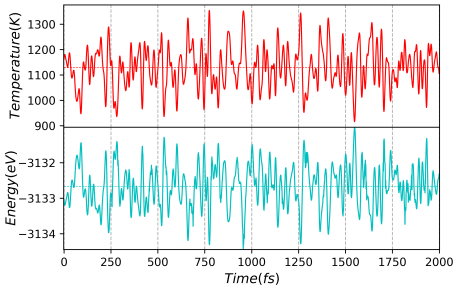

(f) $O_{ba,vac}$

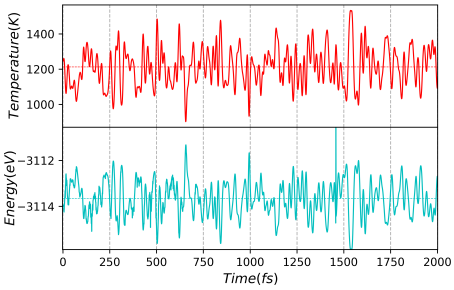

(g) $O_{br,vac}$

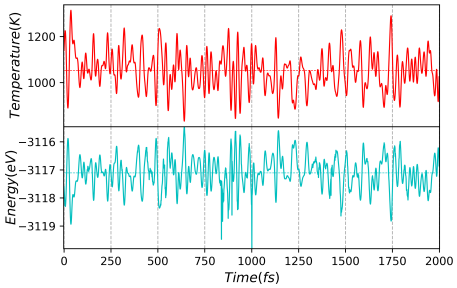

Figure S6: 2ps NVE trajectories initiated at all sites except O_{br}: Temperature (top) and potential energy (bottom).

References

(1) Morgan, B. J.; Watson, G. W. A DFT+ U description of oxygen vacancies at the TiO2 rutile (1 1 0) surface. *Surface Science* **2007**, *601*, 5034–5041.

(2) Kresse, G.; Hafner, J. Ab initio molecular dynamics for liquid metals. *Physical Review B* **1993**, *47*, 558.

(3) Kresse, G.; Hafner, J. Ab initio molecular-dynamics simulation of the liquid-metal–amorphous-semiconductor transition in germanium. *Physical Review B* **1994**, *49*, 14251.

(4) Kresse, G.; Furthmüller, J. Efficiency of ab-initio total energy calculations for metals and semiconductors using a plane-wave basis set. *Computational Materials Science* **1996**, *6*, 15–50.

(5) Kresse, G.; Furthmüller, J. Efficient iterative schemes for ab initio total-energy calculations using a plane-wave basis set. *Physical Review B* **1996**, *54*, 11169.

(6) Sun, J.; Ruzsinszky, A.; Perdew, J. P. Strongly constrained and appropriately normed semilocal density functional. *Physical Review Letters* **2015**, *115*, 036402.

(7) Larsen, A. H.; Mortensen, J. J.; Blomqvist, J.; Castelli, I. E.; Christensen, R.; Dułak, M.; Friis, J.; Groves, M. N.; Hammer, B.; Hargus, C., et al. The atomic simulation environment—a Python library for working with atoms. *Journal of Physics: Condensed Matter* **2017**, *29*, 273002.

(8) Blöchl, P. E. Projector augmented-wave method. *Physical review B* **1994**, *50*, 17953.

(9) Kresse, G.; Joubert, D. From ultrasoft pseudopotentials to the projector augmented-wave method. *Physical Review B* **1999**, *59*, 1758.

(10) Tang, W.; Sanville, E.; Henkelman, G. A grid-based Bader analysis algorithm without lattice bias. *Journal of Physics: Condensed Matter* **2009**, *21*, 084204.

(11) Yu, M.; Trinkle, D. R. Accurate and efficient algorithm for Bader charge integration. *The Journal of Chemical Physics* **2011**, *134*, 064111.

(12) Neugebauer, J.; Scheffler, M. Adsorbate-substrate and adsorbate-adsorbate interactions of Na and K adlayers on Al (111). *Physical Review B* **1992**, *46*, 16067.

(13) Makov, G.; Payne, M. Periodic boundary conditions in ab initio calculations. *Physical Review B* **1995**, *51*, 4014.

(14) Grimme, S.; Antony, J.; Ehrlich, S.; Krieg, H. A consistent and accurate ab initio parametrization of density functional dispersion correction (DFT-D) for the 94 elements H-Pu. *The Journal of Chemical Physics* **2010**, *132*, 154104.

(15) Grimme, S.; Ehrlich, S.; Goerigk, L. Effect of the damping function in dispersion corrected density functional theory. *Journal of Computational Chemistry* **2011**, *32*, 1456–1465.

(16) Iddir, H.; Öğüt, S.; Browning, N. D.; Disko, M. M. Adsorption and diffusion of Pt and Au on the stoichiometric and reduced TiO_2 rutile (110) surfaces. *Physical Review B* **2005**, *72*, 081407.

(17) Hoover, W. G. Canonical dynamics: Equilibrium phase-space distributions. *Physical Review A* **1985**, *31*, 1695.

(18) Mills, G.; Jónsson, H. Quantum and thermal effects in H_2 dissociative adsorption: Evaluation of free energy barriers in multidimensional quantum systems. *Physical Review Letters* **1994**, *72*, 1124.

(19) Henkelman, G.; Jónsson, H. Improved tangent estimate in the nudged elastic band method for finding minimum energy paths and saddle points. *The Journal of Chemical Physics* **2000**, *113*, 9978–9985.

(20) Henkelman, G.; Uberuaga, B. P.; Jónsson, H. A climbing image nudged elastic band method for finding saddle points and minimum energy paths. *The Journal of Chemical Physics* **2000**, *113*, 9901–9904.

(21) Stukowski, A. Visualization and analysis of atomistic simulation data with OVITO–the Open Visualization Tool. *Modelling and Simulation in Materials Science and Engineering* **2009**, *18*, 015012.

(22) Hinuma, Y.; Hayashi, H.; Kumagai, Y.; Tanaka, I.; Oba, F. Comparison of approximations in density functional theory calculations: Energetics and structure of binary oxides. *Physical Review B* **2017**, *96*, 094102.

(23) Ammal, S. C.; Heyden, A. Water-gas shift activity of atomically dispersed cationic platinum versus metallic platinum clusters on titania supports. *ACS Catalysis* **2017**, *7*, 301–309.

(24) Bredow, T.; Pacchioni, G. Electronic structure of an isolated oxygen vacancy at the TiO2 (1 1 0) surface. *Chemical Physics Letters* **2002**, *355*, 417–423.

(25) Landmann, M.; Rauls, E.; Schmidt, W. The electronic structure and optical response of rutile, anatase and brookite TiO2. *Journal of Physics: Condensed Matter* **2012**, *24*, 195503.

(26) Ramamoorthy, M.; King-Smith, R.; Vanderbilt, D. Defects on TiO 2 (110) surfaces. *Physical Review B* **1994**, *49*, 7709.

(27) Lindan, P.; Harrison, N.; Gillan, M.; White, J. First-principles spin-polarized calculations on the reduced and reconstructed TiO 2 (110) surface. *Physical Review B* **1997**, *55*, 15919.

(28) Morgan, B. J.; Watson, G. W. A DFT+ U description of oxygen vacancies at the TiO2 rutile (1 1 0) surface. *Surface Science* **2007**, *601*, 5034–5041.

(29) Matsunaga, K.; Chang, T.-Y.; Ishikawa, R.; Dong, Q.; Toyoura, K.; Nakamura, A.; Ikuhara, Y.; Shibata, N. Adsorption sites of single noble metal atoms on the rutile TiO2 (1 1 0) surface influenced by different surface oxygen vacancies. *Journal of Physics: Condensed Matter* **2016**, *28*, 175002.

(30) Ivanova, E.; Mihaylov, M.; Thibault-Starzyk, F.; Daturi, M.; Hadjiivanov, K. FTIR spectroscopy study of CO and NO adsorption and co-adsorption on Pt/TiO2. *Journal of Molecular Catalysis A: Chemical* **2007**, *274*, 179–184.

(31) Ding, K.; Gulec, A.; Johnson, A. M.; Schweitzer, N. M.; Stucky, G. D.; Marks, L. D.; Stair, P. C. Identification of active sites in CO oxidation and water-gas shift over supported Pt catalysts. *science* **2015**, *350*, 189–192.

(32) Thang, H. V.; Pacchioni, G.; DeRita, L.; Christopher, P. Nature of stable single atom Pt catalysts dispersed on anatase TiO2. *Journal of Catalysis* **2018**, *367*, 104–114.

(33) DeRita, L.; Dai, S.; Lopez-Zepeda, K.; Pham, N.; Graham, G. W.; Pan, X.; Christopher, P. Catalyst architecture for stable single atom dispersion enables site-specific spectroscopic and reactivity measurements of CO adsorbed to Pt atoms, oxidized Pt clusters, and metallic Pt clusters on TiO2. *Journal of the American Chemical Society* **2017**, *139*, 14150–14165.